

See discussions, stats, and author profiles for this publication at: <https://www.researchgate.net/publication/315741966>

History effects and near-equilibrium in adverse-pressure-gradient turbulent boundary layers

Article in *Journal of Fluid Mechanics* · April 2017

DOI: 10.1017/jfm.2017.236

CITATIONS

74

READS

710

4 authors:



Alexandra Bobke

KTH Royal Institute of Technology

8 PUBLICATIONS 175 CITATIONS

[SEE PROFILE](#)



Ricardo Vinuesa

KTH Royal Institute of Technology

190 PUBLICATIONS 1,972 CITATIONS

[SEE PROFILE](#)



Ramis Örlü

KTH Royal Institute of Technology

174 PUBLICATIONS 3,546 CITATIONS

[SEE PROFILE](#)



Philipp Schlatter

KTH Royal Institute of Technology

357 PUBLICATIONS 8,868 CITATIONS

[SEE PROFILE](#)

Some of the authors of this publication are also working on these related projects:



Uncertainty Quantification in CFD and Simulation of Turbulence [View project](#)



New aircraft design paths through control of turbulence [View project](#)

History effects and near-equilibrium in adverse-pressure-gradient turbulent boundary layers

A. Bobke^{1,2}, R. Vinuesa^{1,2†}, R. Örlü¹ and P. Schlatter^{1,2}

¹ Linné FLOW Centre, KTH Mechanics, SE-100 44 Stockholm, Sweden.

² Swedish e-Science Research Centre (SeRC), Stockholm, Sweden.

(Received 2 April 2017)

Turbulent boundary layers under adverse pressure gradients are studied using well-resolved large-eddy simulations (LESs) with the goal of assessing the influence of the streamwise pressure-gradient development. Near-equilibrium boundary layers were characterized through the Clauser pressure-gradient parameter β . In order to fulfil the near-equilibrium conditions, the freestream velocity was prescribed such that it followed a power-law distribution. The turbulence statistics pertaining to cases with a constant value of β (extending up to approximately 40 boundary-layer thicknesses) were compared with cases with non-constant β distributions at matched values of β and friction Reynolds number Re_τ . An additional case at matched Reynolds number based on displacement thickness Re_{δ^*} was also considered. It was noticed that non-constant β cases appear to approach the conditions of equivalent constant β cases after long streamwise distances (around 7 boundary-layer thicknesses). The relevance of the constant β cases lies in the fact that they define a “canonical” state of the boundary layer, uniquely characterised by β and Re . The investigations on the flat plate were extended to the flow around a wing section overlapping in terms of β and Re . Comparisons with the flat-plate cases at matched values of β and Re revealed that the different development history of the turbulent boundary layer on the wing section leads to a less pronounced wake in the mean velocity as well as a weaker second peak in the Reynolds stresses. This is due to the weaker accumulated effect of the β history. Furthermore, a scaling law suggested by Kitsios *et al.* (Int. J. Heat Fluid Flow, 2016), proposing the edge velocity and the displacement thickness as scaling parameters, was tested on two constant-pressure-gradient parameter cases. The mean velocity and Reynolds-stress profiles were found to be dependent on the downstream development. The present work is the first step towards assessing history effects in adverse-pressure-gradient turbulent boundary layers and highlights the fact that the values of the Clauser pressure-gradient parameter and the Reynolds number are not sufficient to characterise the state of the boundary layer.

Key words: Turbulent boundary layers, Numerical simulations

1. Introduction

Turbulent boundary layers (TBLs) subjected to streamwise pressure gradients (PGs) are of great importance in a wide range of industrial applications, including the flow around a wing or inside a diffuser. Despite their relevance, the effects of PGs on the

† Email address for correspondence: rvinuesa@mech.kth.se

characteristics of wall-bounded turbulence are still elusive. Part of the reason for this lack of detailed knowledge of PG TBLs is the fact that there is not a systematic approach towards characterizing the pressure gradient. Since the effect of the pressure gradient on the TBL is closely related to its streamwise development (Spalart & Watmuff 1993), it is important to define the concept of an *equilibrium* boundary layer: according to the strict definition by Townsend (1956), this condition requires the mean flow and Reynolds-stress tensor profiles to be independent of the streamwise position x , when scaled with appropriate local velocity and length scales. As also shown by Townsend (1956) this condition is only satisfied by the sink flow, although it is possible to define a less restrictive *near-equilibrium* condition when the mean velocity defect $U_\infty - U$ is self-similar in the outer region, which in any case dominates at high Reynolds numbers (Marusic *et al.* 2010). Townsend (1956) and Mellor & Gibson (1966) showed that these near-equilibrium conditions can be obtained when the freestream velocity is prescribed by a power law such that $U_\infty = C(x - x_0)^m$, where C is a constant, x_0 is a virtual origin and m the power-law exponent. In particular, Townsend (1956) showed that m has to be larger than $-1/3$ in order to obtain near-equilibrium conditions, which means that all accelerated TBLs subjected to a favorable pressure gradient (FPG), with U_∞ distributions defined by a power law, exhibit near-equilibrium. Regarding TBLs subjected to adverse pressure gradients (APGs), only the ones with U_∞ defined by a power law as defined above, and satisfying $-1/3 < m < 0$ are in near-equilibrium conditions. Note that Townsend (1956) also showed that a freestream velocity distribution defined by an exponential function as $U_\infty = C \exp(\mu x)$ (with μ being a constant) may also lead to near-equilibrium conditions, although only if $\mu > 0$, *i.e.*, only in the case of FPG TBLs. Further discussion on equilibrium in APG TBLs can be found in the work by Maciel *et al.* (2006). An additional interesting conclusion is the fact that the widely studied zero-pressure-gradient (ZPG) TBL (Schlatter *et al.* 2009; Bailey *et al.* 2013), driven by a constant freestream velocity, is a particular case of the general near-equilibrium TBLs proposed by Townsend (1956) and Mellor & Gibson (1966) where $m = 0$. In this respect, it is relatively common in the literature to refer to “self-similar” boundary layers, where as discussed above the only case in which complete self-similarity is observed is the sink flow. For instance, Skåre & Krogstad (1994) obtained an experimental APG TBL with a U_∞ distribution given by a power law, and with $m = -0.23$, which in principle would lead to near-equilibrium conditions. Nevertheless, the authors described their boundary layer as a self-similar one, therefore there is some discrepancy in the terminology and interpretation of PG TBL data. Moreover, power-law distributions of U_∞ were also considered in the numerical studies by Skote *et al.* (1998), Lee & Sung (2009) and Lee (2017), focused on attached APG TBLs, and by Skote & Henningson (2002) where the aim was to characterize separated APG TBLs. In this context, the connection between backflow events present in APG TBLs and the mechanisms of separation have recently been studied by Vinuesa *et al.* (2017).

These differences in terminology are motivated in part by the difficulties arising from setting up canonical PG TBLs, the wide range of parameters used to characterize pressure-gradient effects (Monty *et al.* 2011), as well as the impact of history effects on the local state of the TBL (Schlatter & Örlü 2012), which leads to additional difficulties in the interpretation of the results. Another factor that might as well have contributed to the confusion when it comes to turbulence quantities, is the different level of insufficient spatial resolution (Hutchins *et al.* 2009).

Perry *et al.* (2002) attempted to develop a methodology to compute mean flow, Reynolds stress components and total shear-stress profiles, for any given freestream velocity distribution. Although this is a challenging task, especially in the general non-equilibrium case

they considered, they reached some success with several empirical closures, and acknowledged the lack of data in the literature to accurately compute such streamwise evolutions. They identified the most relevant parameters determining the flow evolution from a particular initial condition, and considered a wide range of cases, from APG TBLs to the sink flow. More recently, a simplified version of the framework developed by Perry *et al.* (2002) was used by Marusic *et al.* (2015) to evaluate the downstream evolution of ZPG TBLs from various initial conditions, in particular to assess the convergence towards a canonical ZPG configuration from different tripping devices.

The focus of this study is on near-equilibrium APG TBLs, and more precisely on the assessment of history effects on the boundary-layer development. To that end, we consider the Clauser pressure-gradient parameter $\beta = \delta^* / \tau_w dP_\infty / dx$, where δ^* is the displacement thickness, τ_w is the wall-shear stress and P_∞ is the freestream pressure, to quantify the pressure-gradient magnitude and evaluate the evolution of flat-plate TBLs under various $\beta(x)$ distributions. For this purpose, datasets from well-resolved large-eddy simulations (LESs) of turbulent boundary layers with various APG conditions (Bobke *et al.* 2016b) and the flow over the suction side of a wing from a recent direct numerical simulation (DNS) (Hosseini *et al.* 2016) are considered. To complement the existing databases, two new simulations in which the pressure-gradient parameter β remains constant have been performed. To the best of the authors knowledge, this is the first systematic approach to assess the effect of streamwise pressure-gradient history effects on the development of turbulent boundary layers.

The paper is organized as follows: in §2 we provide a description of the numerical method used for the flat-plate APG simulations, as well as a summary of the various databases under consideration; the impact of different $\beta(x)$ distributions on turbulence statistics, spectra and boundary-layer development is discussed in §3; in §4 we use our cases with constant β to assess the alternative scaling law proposed by Kitsios *et al.* (2016); and finally in §5 the main conclusions of the present study are outlined.

2. Numerical method and databases

The downstream evolution of TBLs subjected to adverse pressure gradients was studied by means of well-resolved large-eddy simulations (LESs). The pressure gradient was imposed through the variation of the freestream velocity at the top of the domain, which was defined following the near-equilibrium definition by Townsend (1956), *i.e.*, $U_\infty(x) = C(x - x_0)^m$. Thus, different near-equilibrium boundary layers were investigated by varying the virtual origin x_0 and the power-law exponent m as listed in Table 1.

We used the code SIMSON (Chevalier *et al.* 2007), which is based on a fully-spectral method with Fourier discretisation in streamwise and spanwise directions and on the Chebyshev-tau method in the wall-normal direction. See also the work by Skote (2001) for additional details on APG TBL simulations with this code. A summary of the simulation parameters, including domain size and grid resolutions for the various cases, is given in Table 2. Note that in this article the superscript ‘+’ denotes inner scaling, *i.e.*, nondimensionalization with the friction velocity $u_\tau = \sqrt{\tau_w / \rho}$ (where τ_w is the wall-shear stress and ρ is the fluid density) and the fluid kinematic viscosity ν . The value of u_τ used to compute the grid resolutions reported in Table 2 was taken at $x/\delta_0^* = 250$ (where δ_0^* is the displacement thickness of the laminar inflow) in all the cases. In this work we used the approximate deconvolution relaxation-term model (ADM-RT, see Schlatter *et al.* 2004) as a sub-grid scale (SGS) model as in Eitel-Amor *et al.* (2014). Unlike other SGS models, in the relaxation-term approach the forcing acts directly on the resolved

velocity components \bar{u}_i ,

$$\frac{\partial \tau_{ij}}{\partial x_j} = \chi H_N * \bar{u}_i, \quad (2.1)$$

where τ_{ij} denotes the Reynolds stresses, χ is a model coefficient which is taken as equal to 0.2, and the cut-off frequency of the high-order filter H_N is taken as $\omega_c \approx 0.86\pi$. The high-order filter H_N is designed so that the model affects only the small scales in the flow, whereas the large scales are unaffected by the model. The symbol $*$ represents the convolution operator, and the overbar the implicit grid filter due to the lower resolution in the LES. In earlier boundary-layer studies (Eitel-Amor *et al.* 2014; Bobke *et al.* 2016a) it has been shown that the results from the LES are in very good agreement with the DNS in terms of mean velocity, Reynolds-stress tensor and turbulence budgets. At the wall a no-slip condition was imposed, while at the upper boundary a Neumann condition was applied. In particular, we set $\partial u / \partial y = \partial w / \partial y = 0$, and the wall-normal velocity gradient is obtained from continuity as $\partial v / \partial y = -\partial U_\infty / \partial x$, therefore the freestream velocity distribution is imposed through the Neumann boundary condition. Although technically this choice of boundary conditions does not lead to zero spanwise vorticity ω_z in the freestream, we have observed that ω_z is approximately zero well beyond the boundary-layer edge (for $y > 2.5\delta_{99}$, where δ_{99} is the 99% boundary-layer thickness), and only very close to the top boundary increases slightly to match the condition $\partial u / \partial y = 0$ (Bobke *et al.* 2016b). In order to ensure periodic boundary conditions in the streamwise direction a fringe region was considered upstream of the outlet, which forces the fully-turbulent flow back to the laminar Blasius inlet profile. The pressure gradients in the TBLs under consideration are of different magnitudes, and exhibit various streamwise developments. The resulting pressure-gradient parameter β decreases over the streamwise direction in the cases *m13*, *m16* and *m18*, whereas β remains constant over streamwise distances of $37\bar{\delta}_{99}$ and $28\bar{\delta}_{99}$ in the cases *b1* and *b2*, respectively. The overbar denotes the boundary-layer thickness averaged over the region where β is observed to remain constant. The determination of the boundary-layer thickness and edge velocity can become ambiguous and cumbersome the stronger the pressure gradient becomes, hence, here the 99% boundary-layer thickness δ_{99} was determined by means of the method developed by Vinuesa *et al.* (2016) for PG TBLs. Further details regarding the numerical setup of the cases *m13*, *m16* and *m18* are given by Bobke *et al.* (2016b). In addition to the five flat-plate APG cases discussed above, also the TBL developing over the suction side of a NACA4412 wing section at $Re_c = 400,000$ (where Re_c is the Reynolds number based on freestream velocity U_∞ and chord length c) by Hosseini *et al.* (2016), and the ZPG TBL data by Schlatter *et al.* (2009) are considered, as shown in Table 1. The idea is that the TBL developing on the suction side of the wing is subjected to a progressively stronger APG (contrary to the flat-plate APG TBLs, in which case they are either constant or mildly relaxing), and therefore exhibits a very interesting $\beta(x)$ distribution, which will enrich the comparison with the near-equilibrium cases developing over the flat plate. DNS was considered for the wing case, and the spectral-element code Nek5000 (Fischer *et al.* 2008) was employed, as discussed in detail in Hosseini *et al.* (2016). The DNS of ZPG TBL by Schlatter *et al.* (2009) is considered to provide a baseline case, with respect to which pressure-gradient effects can be assessed, since the APG cases start from the same initial conditions as the ZPG case.

2.1. Effect of the SGS model on the dissipation of turbulent kinetic energy

As stated above, in the present study we performed well-resolved LESs, which means that the resolutions reported in Table 2 are good, although not as high as the ones considered








Case	Type	Reynolds-number range	m	x_0	β	Color code
$m13$	LES	$990 < Re_\theta < 3515$	-0.13	60	[0.86; 1.49]	
$m16$	LES	$1010 < Re_\theta < 4000$	-0.16	60	[1.55; 2.55]	
$m18$	LES	$990 < Re_\theta < 4320$	-0.18	60	[2.15; 4.07]	
$b1$	LES	$910 < Re_\theta < 3360$	-0.14	110	$\simeq 1$	
$b2$	LES	$940 < Re_\theta < 4000$	-0.18	110	$\simeq 2$	
Wing	DNS	$790 < Re_\theta < 2800$	—	—	[0.61; 85]	
ZPG	DNS	$770 < Re_\theta < 2500$	0	0	$\simeq 0$	

TABLE 1. List of datasets used in the present paper, including their momentum-loss Reynolds number range, power-law exponent, virtual origin, Clauser pressure-gradient parameter and color code used throughout the remainder of the paper. The setup of cases $m13$, $m16$ and $m18$ is reported in detail by Bobke *et al.* (2016b); the Wing case is described by Hosseini *et al.* (2016), and the ZPG database is reported by Schlatter *et al.* (2009). Note that the ranges are given for $x > 500$, and up to the location where the fringe in the outflow is applied.

Case	L_x/δ_0^*	L_y/δ_0^*	L_z/δ_0^*	Δx^+	Δy_{\max}^+	Δz^+	N_x	N_y	N_z
$m13$	3000	120	160	21.6	13.9	9.2	3072	301	384
$m16$	3000	180	220	21.2	17.0	8.3	3072	361	576
$m18$	3000	250	320	21.2	21.3	9.0	3072	401	768
$b1$	3000	140	250	21.2	16.4	9.7	3072	301	576
$b2$	3000	180	320	21.6	17.4	9.2	3072	361	768

TABLE 2. Summary of simulation parameters from the various cases considered in this study. L_x , L_y and L_z are the domain sizes in the streamwise, wall-normal and spanwise directions. Δx and Δz are the collocation resolutions in the wall-parallel directions, obtained using N_x and N_z points, respectively. Δy_{\max} is the maximum grid spacing in the wall-normal direction and the number of Chebyshev polynomials is denoted by N_y . Note that in all the cases, at least 10 grid points were located below $y^+ = 10$.

in proper DNS. As in the work by Eitel-Amor *et al.* (2014) we use the ADM-RT subgrid-scale model by Schlatter *et al.* (2004), which adds an additional dissipation at the smallest scales, with the aim of improving the accuracy of the results. Eitel-Amor *et al.* (2014) performed well-resolved LESs of the ZPG TBL case up to $Re_\theta = 8300$, and compared the terms in the turbulent kinetic energy (TKE) budget from their LES with the ones in the DNS simulation of a ZPG TBL at $Re_\theta = 3600$ (Schlatter & Örlü 2010). Their results revealed that the agreement in all the terms of the TKE budget was excellent, and in fact when adding their resolved dissipation of TKE (which amounted to 87.2% of the total dissipation in the DNS) with the additional dissipation of the SGS model, they were able to recover 99.8% of the total dissipation from the DNS. The results by Eitel-Amor *et al.* (2014) in ZPG TBLs, using the same SGS approach as the one reported here, show the

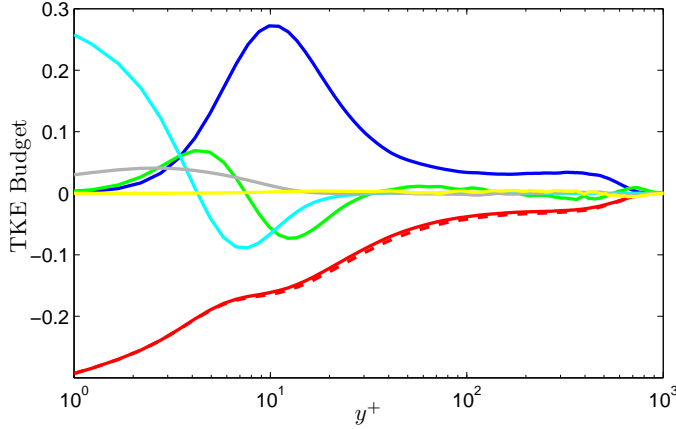


FIGURE 1. TKE budget corresponding to the *m13* case at $x \simeq 2200$. The Reynolds number based on momentum thickness is $Re_\theta = 3300$, and the value of β is around 0.93. The budget terms are represented as follows: — production, — resolved dissipation, — turbulent transport, — viscous diffusion, — velocity-pressure-gradient correlation and — convection. Note that the total dissipation, including the resolved component and the additional contribution from the SGS model, is represented by - - -. The TKE budget terms are scaled by u_τ^4/ν .

adequacy of the method considered in the present study. Moreover, in this section we illustrate the effect of the SGS model in APG TBLs. Note that the transport equation of the TKE, defined as $k = 1/2(\langle u^2 \rangle + \langle v^2 \rangle + \langle w^2 \rangle)$, is given by:

$$\frac{\partial k}{\partial t} = P^k + \varepsilon^k + D^k + \Pi^k + T^k + C^k, \quad (2.2)$$

where the production term is computed as $P^k = -\langle u_i u_j \rangle \partial U_i / \partial x_j$, the dissipation as $\varepsilon^k = -2\nu \langle s_{ij} s_{ij} \rangle$ (where s_{ij} fluctuating strain rate), the viscous diffusion is defined as $D^k = (\nu/2) \partial^2 \langle u_i u_i \rangle / \partial x_j^2$, the velocity-pressure-gradient correlation is $\Pi^k = -(1/\rho) \partial \langle p u_i \rangle / \partial x_i$, the turbulent transport is calculated as $T^k = -(1/2) \partial \langle u_i u_i u_j \rangle / \partial x_j$, and the convection is $C^k = -(1/2) \langle u_j \rangle \partial \langle u_i u_i \rangle / \partial x_j$. In Figure 1 we show the TKE budget corresponding to the *m13* case at $Re_\theta = 3300$, subjected to a value of $\beta \simeq 0.93$. Although the effects of the APG on the various terms from the TKE budget are discussed in detail in §3.2 for various pressure-gradient conditions, here it is interesting to highlight that the resolved dissipation corresponds to 92% of the total dissipation. Note that the total dissipation would also include the additional contribution from the SGS model. Note that the larger percentage of resolved dissipation, compared to the ZPG case, can be explained by the fact that the friction velocity values used to design the mesh were taken at $x \simeq 250$, whereas the budget shown in Figure 1 was extracted at $x \simeq 2200$. Naturally, the friction-velocity value at the location where the budget is obtained is lower than the one used to design the mesh due to the APG, and consequently the resolution is effectively higher. Therefore, we consider that the resolution and SGS model used in the present study are adequate to properly reproduce the energy transfer across scales in the present APG TBLs.

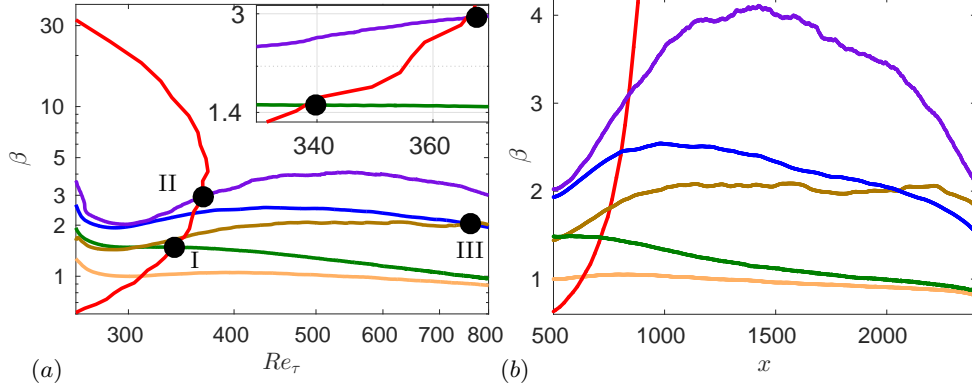


FIGURE 2. Clauser pressure-gradient parameter β as function of (a) friction Reynolds number Re_τ and (b) streamwise coordinate x for the following cases: — boundary layer developing on the suction side of a wing (Hosseini *et al.* 2016), and over a flat plate for non-constant β -cases (— $m = -0.13$, — $m = -0.16$ and — $m = -0.18$) and constant β -cases (— $\beta = 1$ and — $\beta = 2$). Inset and black dots indicate the matched $\beta - Re_\tau$ values that will be considered in the remainder of the paper.

3. Results and discussion

3.1. Streamwise development

We first report the streamwise development of five near-equilibrium APG TBLs on flat plates, defined by different power-law exponents and virtual origins. As stated in §1, the state of the boundary layer will not depend on the particular value of β at a certain position, but on its development history, *i.e.*, on $\beta(x)$. While β decreases over the streamwise direction in the cases denoted with m ($m13$, $m16$, $m18$), β remains constant for the two cases denoted with b ($b1$, $b2$). Let us recall that although β is not constant with x in the m cases, these TBLs are in near-equilibrium due to the fact that the U_∞ distribution is prescribed by a power law as defined by Townsend (1956) and Mellor & Gibson (1966). Regarding the cases with constant β , not only are they in near-equilibrium, but they also allow a better characterization of Reynolds-number effects in a certain pressure-gradient configuration. Note that the ZPG TBL flow essentially corresponds to a constant $\beta = 0$ configuration. In Figure 2 we show the streamwise evolution of β , as a function of the friction Reynolds number Re_τ (based on the friction velocity u_τ and the boundary-layer thickness δ_{99}) and the streamwise coordinate x , for the various flat-plate cases as well as for the TBL on the suction side of a wing described in §2. For the flat-plate cases the inflow laminar displacement thickness δ_0^* is used to nondimensionalise x , whereas for the case of the wing the displacement thickness at $x/c = 0.15$, where the flow is post-transitional, is considered.

Further insight into the characteristics of near-equilibrium TBLs can be gained by analyzing the streamwise evolution of the defect shape factor G , defined as follows:

$$G = \frac{\int_0^\infty (U_\infty^+ - U^+)^2 dy}{\int_0^\infty (U_\infty^+ - U^+) dy}. \quad (3.1)$$

Note that the defect shape factor can also be expressed as $G = (H_{12} - 1) / (H_{12} \sqrt{c_f/2})$, where $c_f = 2(u_\tau/U_e)^2$ is the skin-friction coefficient (with U_e being the boundary-layer edge velocity at the particular streamwise location) and $H_{12} = \delta^*/\theta$ is the shape factor. According to Mellor & Gibson (1966), the value of G is essentially constant in near-

equilibrium APG TBLs with a constant value of β , and they also introduced a correction factor for G at low Reynolds numbers. In Figure 3 we show the streamwise evolution of G in the various cases under consideration, including the ZPG TBL. It is interesting to note that, as expected from the work by Mellor & Gibson (1966), the values of G generally increase for progressively larger values of β , and qualitatively the $G(x)$ curves resemble the $\beta(x)$ ones. Moreover, it is interesting to observe that the cases with regions of constant β , *i.e.*, the ZPG TBL and the $b1$ and $b2$ APGs, also exhibit regions of constant G , which is also in agreement with Mellor & Gibson (1966). Note that in Figure 2(b) it can be observed that the $b1$ case shows a region of constant $\beta = 1$ in the range $500 < x < 1300$, whereas in the $b2$ configuration the $\beta = 2$ region is identified for $1000 < x < 2300$. On the other hand, the results shown in Figure 3 reveal that the regions of constant G start downstream of the corresponding regions of constant β : in the $b1$ case the constant- G region starts at around $x \simeq 1000$, and in the $b2$ configuration it starts at around $x \simeq 1200$. Interestingly, these regions of constant defect shape factor end at approximately the same locations as the constant- β regions do. Moreover, the ZPG case appears to exhibit a region of constant G already at $x \simeq 500$, and it extends up to $x \simeq 2300$. A possible explanation for the delay in the region of constant G present in the APG cases can be the fact that, as stated by Mellor & Gibson (1966), G is essentially constant in regions of constant β but there is a small Reynolds-number effect, which is only significant at low Reynolds numbers. A correction to account for this effect was proposed by Mellor & Gibson (1966), and the correction leads to an increase in G inversely proportional to the Reynolds number and the skin-friction coefficient. Since, as discussed below, the ZPG case exhibits larger c_f values than the APG ones, the correction would have a smaller effect on this case, thus explaining the reason why this configuration exhibits the constant- G behavior earlier. Moreover, the fact that the two APG cases also exhibit regions of constant G is attributed to the fact that the correction only has a significant contribution at low Reynolds numbers. Note that Mellor & Gibson (1966) provided theoretical predictions of the values of G in PG TBLs subjected to different values of β . In particular, in Table 3 we provide a comparison of the G values obtained in the constant- G regions from the $\beta = 0, 1$ and 2 cases in the present study, with the values reported by Mellor & Gibson (1966). The values are in reasonably good agreement, especially at lower values of β , and the general increasing trend of G with β predicted by Mellor & Gibson (1966) is also well represented by the present numerical simulations. It is also important to note that, as indicated in §1, the fact that a TBL exhibits a constant value of β , or of G , does not imply that this boundary layer exhibits self-similarity, since as shown by Townsend (1956) only the sink flow fulfils the requirements for complete self-similarity. On the other hand, the constant- β cases (including the ZPG TBL) are particular cases of near-equilibrium PG TBLs, in which the mean velocity defect is self-similar in the outer region at high Reynolds numbers (Marusic *et al.* 2010). The scaling of near-equilibrium TBLs is further discussed in §4.

The streamwise development of various integral quantities, for the various configurations under consideration, is discussed next. In Figure 4(a), Re_τ is shown for all pressure-gradient cases listed in Table 1. The growth of Re_τ is similar for all the boundary layers over the flat plate reaching up to $Re_\tau \simeq 900$ at the end of the domain. The APG was applied at the streamwise position $x \simeq 350$, which is denoted by the vertical line. At this position a change in the slope of Re_τ can clearly be observed between the various APG TBLs. Interestingly, the Re_τ trend appears to be relatively independent of the strength of the pressure gradient in the investigated β -range. Note that in the case of the APG TBL developing on the suction side of a wing the growth of Re_τ is also similar to the flat-plate cases up to $Re_\tau \simeq 380$, from where on Re_τ decreases rapidly towards the trailing edge of

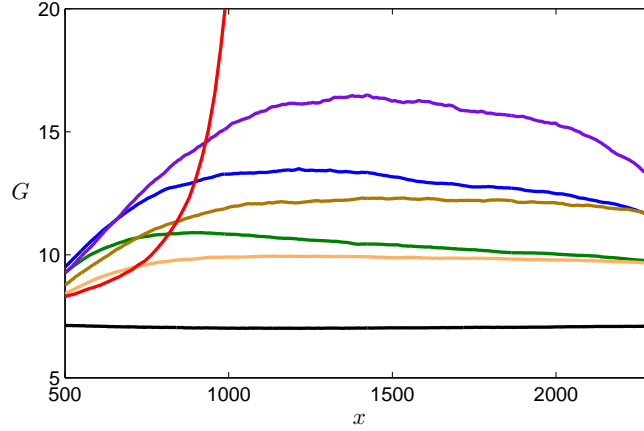


FIGURE 3. Streamwise evolution of the defect shape factor G , defined in equation (3.1), for the various cases under consideration in this work. The color code is given in Table 1.

Value of β	Mellor & Gibson (1966)	Present study
0	6.6	7.0
1	9.2	9.8
2	11.1	12.1

TABLE 3. Summary of values of G obtained in the constant- β regions from the cases with $\beta = 0, 1$ and 2 in the present study, compared with the theoretical predictions by Mellor & Gibson (1966).

the wing due to the progressively stronger values of β obtained in this region. Towards the trailing edge of the wing, the skin friction is further reduced and with this the friction velocity u_τ and Re_τ , despite the relative increase in δ_{99} . Also, let us recall that for the wing we show results for $x/c > 0.15$ (since the flow is tripped at $x/c = 0.1$), and the value of δ^* at this location is used to nondimensionalize the streamwise coordinate x . Moreover, in Figure 4(b) the Reynolds number based on the momentum thickness Re_θ is shown. Within the ZPG region the various flat-plate cases exhibit very good agreement, and grow within the APG region with various growth rates depending on the particular $\beta(x)$ distribution. Note that in general the cases subjected to larger $\beta(x)$ values show larger Re_θ , due to the increase in the boundary-layer thickness produced by the boundary layer lift up caused by the APG. The growth of Re_θ in the wing is comparable to the one observed in the flat-plate case up to $x \simeq 900$. Beyond this point, the Re_θ curve exhibits a stepper growth rate. The value of β at the streamwise position where the Re_τ and Re_θ curves from the wing start to deviate from those of the flat-plate cases is around 4, beyond those considered in the comparison of statistics from §3.2.

In Figure 5 we show the skin-friction coefficient c_f and the shape factor H_{12} as a function of Re_θ for the various APG cases. Firstly, the c_f trends from the APG boundary layers are below the ZPG correlation by Nagib *et al.* (2007), which is explained by the reduced velocity gradient at the wall and is a consequence of the increased thickening

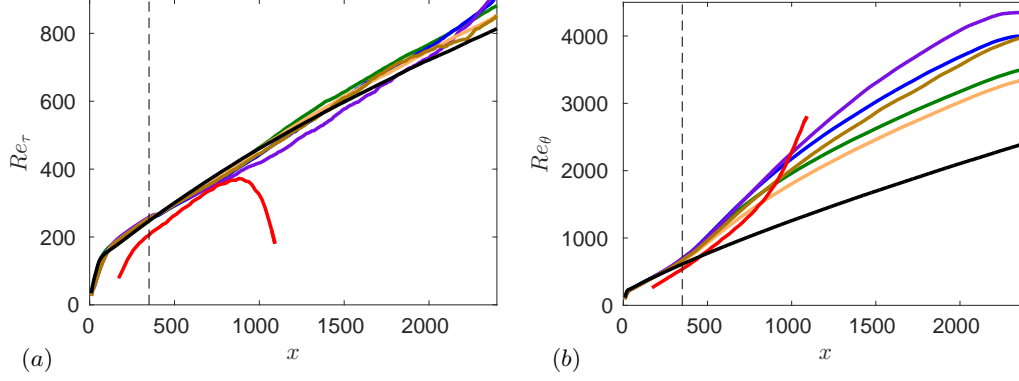


FIGURE 4. Streamwise evolution of (a) friction Reynolds number Re_τ and (b) momentum-loss Reynolds number Re_θ . The location where the pressure gradient is applied, $x = 350$, is represented by a thin dashed line and the colors are given by Table 1.

experienced by the boundary layer in the streamwise direction due to the action of the APG. This is also connected to the higher U_∞^+ values observed in the APG boundary layers, as discussed in §3.2. Also note that the various APG cases exhibit similar c_f evolutions in the range $350 < Re_\theta < 1000$, whereas at higher Reynolds numbers the development is strongly influenced by the particular $\beta(x)$ distribution. It can be observed in Figure 5(a) that higher β values lead to lower skin friction. Moreover, the agreement among profiles for $350 < Re_\theta < 1000$ is associated with the fact that the boundary layer needs a certain streamwise distance to adapt to the prescribed APG conditions, since the $U_\infty(x)$ distribution leading to the APG is imposed at the top boundary of the computational domain, but its effect in c_f is reflected at the wall. On the other hand, within the ZPG region, the given correlation does not represent the data of the simulations, which can be explained by the way that the pressure gradient is introduced in the flow: the freestream velocity profile is modified according to the corresponding power law, but the ZPG region is not long enough to reach a canonical ZPG state, which is represented by the correlation from Nagib *et al.* (2007); similar observations have been made by Schlatter & Örlü (2010). In this context, it is interesting to point out that the wing boundary layer actually reaches the c_f values from the ZPG correlation at $Re_\theta \simeq 350$, and deviates from it at around $Re_\theta \simeq 700$. The boundary layer developing on the suction side of the wing starts from very low values of $\beta \simeq 0$, and therefore exhibits a region of approximate ZPG conditions, which allows a development closer to that of canonical ZPGs, before the exponential increase in β observed beyond $x/c \simeq 0.4$ (Hosseini *et al.* 2016). Similar conclusions can be drawn from the streamwise evolution of the shape factor H_{12} , shown in Figure 5(b). Whereas the curves from the various APG cases collapse for $350 < Re_\theta < 1000$, H_{12} grows more rapidly for higher β than for the small and intermediate β cases, where actually a small decrease can be detected towards high Re_θ . Note that higher β values lead to larger H_{12} due to the fact that an APG boundary layer will be thicker than an equivalent ZPG carrying the same momentum. Nevertheless, the distribution of H_{12} in ZPGs differs completely to the one in APG TBLs, not even the slopes in the range $350 < Re_\theta < 1000$ are similar. This is also connected to the thicker boundary layers in APG flows, and the lift-up of the boundary layer. It is also interesting to note that the wing boundary layer exhibits a similar trend to that of the various flat-plate cases up to $x \simeq 1000$, after which point the significantly higher increase in β leads to a much steeper growth in shape factor. Most notable is, however,

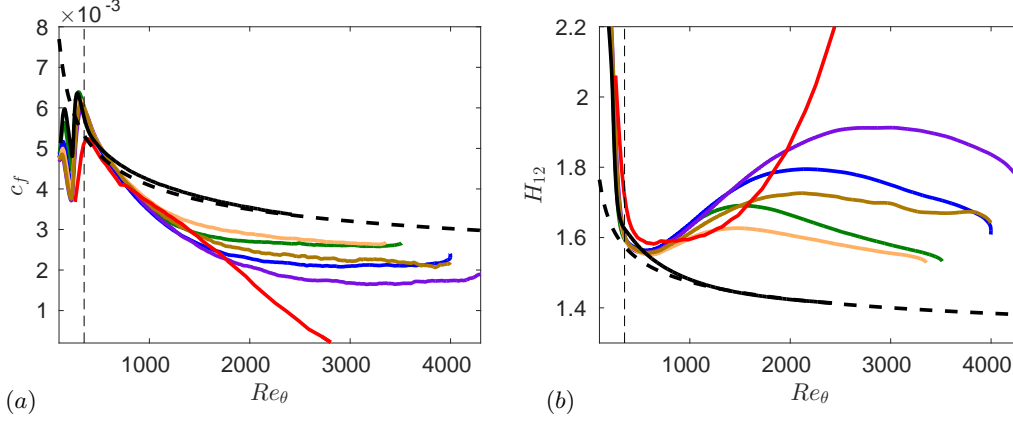


FIGURE 5. Evolution of (a) skin-friction coefficient c_f and (b) shape factor H_{12} with momentum-loss Reynolds number Re_θ . ---- represents the empirical correlations developed by Nagib *et al.* (2007) for c_f , and by Monkewitz *et al.* (2007) for H_{12} . The location where the pressure gradient is applied, $x = 350$, is represented by a thin dashed line and the colors are given by Table 1.

Re_θ -trend exhibited by the constant β cases $b1$ and $b2$, in which both the skin-friction coefficient and shape factor curves are nearly parallel to the ZPG, *i.e.*, $\beta = 0$, case.

The effect of the particular $\beta(x)$ distributions on the turbulence statistics, for the various cases under consideration, is discussed next.

3.2. Effect of history on turbulence statistics

In order to evaluate the impact of different $\beta(x)$ distributions on the local state of the APG TBL, we select three cases in which the β and Re_τ conditions are matched, but with different streamwise histories of β . As highlighted with black dots in Figure 2, the first selected case is $\beta = 1.4$ and $Re_\tau = 340$, obtained from the wing (which starts from very low values of β and exhibits approximately exponential growth with x) and from the flat-plate case $m13$ (in which a decreasing trend in β , starting from higher values, is observed). The second case exhibits a slightly higher friction Reynolds number $Re_\tau = 367$, at a stronger adverse pressure gradient $\beta = 2.9$, and in this case also the wing is selected (with the exponentially increasing $\beta(x)$), together with the flat-plate APG case $m18$, which at that point exhibits a slightly increasing trend in β . The third case highlighted in Figure 2 involves the two flat-plate APG TBLs $m16$ and $b2$, at a higher Reynolds number of $Re_\tau = 762$, and with $\beta = 2.0$. Note that in this particular case both boundary layers are in near-equilibrium, and that the $b2$ configuration exhibits a constant value of $\beta = 2$ starting at $x \simeq 1000$, whereas in the $m16$ case the β curve shows a decreasing trend. Additionally, ZPG profiles at the corresponding Re_τ are shown together with each of the comparisons.

In Figure 6 we show the inner-scaled mean flow for the various comparisons discussed above, as well as selected components of the Reynolds-stress tensor. The first two important observations from this figure are: although the three comparisons are at the same β and Re_τ , the turbulence statistics in the outer layer (*i.e.*, overlap and wake layers) are essentially different among the cases, while they agree in the viscous sublayer, *i.e.*, for $y^+ < 5$. This highlights the significant impact of history effects on the state of the outer layer of a turbulent boundary layer. Focusing on Figure 6(a), we can observe the general effect of a moderate APG with $\beta = 1.4$ on the boundary layers, compared with the equivalent ZPG case: the APG TBLs exhibit a steeper logarithmic region, as previously

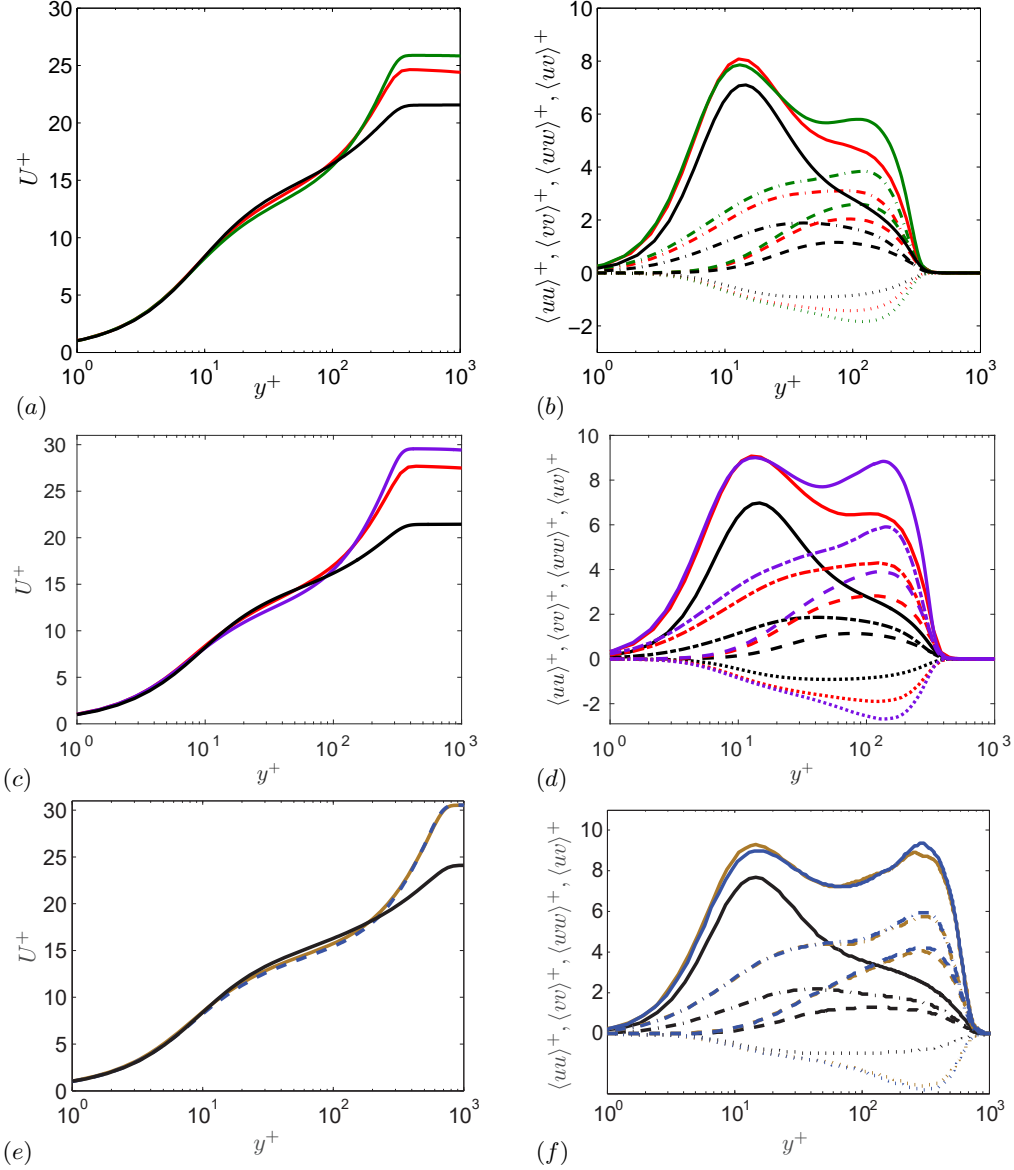


FIGURE 6. (a), (c), (e) Inner-scaled mean velocity profiles and (b), (d), (f) selected components of the inner-scaled Reynolds-stress tensor. (a), (b) correspond to case I: $\beta = 1.4$ and $Re_\tau = 340$; (c), (d) to case II: $\beta = 2.9$ and $Re_\tau = 367$; and (e), (f) to case III: $\beta = 2.0$ and $Re_\tau = 762$. Colors as in Table 1, and the following line styles correspond to the various Reynolds-stress tensor components: — $\langle uu \rangle^+$, ---- $\langle vv \rangle^+$, -.- $\langle ww \rangle^+$ and $\langle uv \rangle^+$. The dotted line in (e) is used to allow better visualization of the profiles.

observed by Nagib & Chauhan (2008) who reported lower values of the von Kármán coefficient κ in APGs. Moreover, the APG TBLs also exhibit a more prominent wake than the ZPG, associated with stronger energetic structures in the outer region, as also observed by Monty *et al.* (2011) and Vinuesa *et al.* (2014). With respect to the differences between the two APG cases, it is important to recall that the profiles on the suction side of the wing were obtained by means of DNS, whereas the flat-plate boundary layers

are based on LES. This could be the reason for the subtle discrepancies between both profiles in the buffer region, since as documented by Eitel-Amor *et al.* (2014) the coarser resolution used in the LES produces slightly lower mean velocities in this region of the boundary layer. Nevertheless, the effect of the LES is negligible in the outer region, and therefore the differences observed in the wake of the two APG cases can be attributed to their particular streamwise evolution. Monty *et al.* (2011) and Harun *et al.* (2013) showed that the APG energizes the largest turbulent structures in the outer flow, leading to the more prominent wake, as well as to the outer peak in the streamwise velocity fluctuation profile. As noticeable in Figure 2, the $\beta(x)$ curve from the $m13$ case exhibits values above 1.4 from the start of the pressure-gradient region, whereas in the wing the initial β values are close to zero, and they only reach the value 1.4 after a certain streamwise development. Therefore, in the $m13$ case the outer flow was subjected to a stronger APG throughout its streamwise development, and hence the larger structures received much more energy from the APG. As a consequence, and although at $Re_\tau = 340$ the wing and the flat-plate boundary layers have the same value of $\beta = 1.4$, the accumulated $\beta(x)$ effect leads to a stronger impact of the APG in the $m13$ case. The Reynolds-stress tensor components are analyzed for this case in Figure 6(b), where again the most characteristic features of APG TBLs can be observed in comparison with the ZPG case (Monty *et al.* 2011): the streamwise velocity fluctuation profile develops an outer peak, a consequence of the energizing of the large-scale motions, which also produces an increase of the near-wall peak due to the connection between the near-wall region and the outer flow. Note that the location of this inner peak, $y^+ \simeq 15$, is essentially unaffected by the APG. The wall-normal and spanwise velocity variance profiles, as well as the Reynolds shear-stress profile, exhibit a more prominent outer region compared to the ZPG due to the effect of the APG on the outer flow. Regarding the characteristics of the two APG cases, the first noticeable feature is the fact that the value of the inner peak appears to be approximately the same in the two cases, whereas the $m13$ case exhibits a stronger outer peak. The larger value of the outer peak can be explained, as well as the more prominent wake, by the fact that the flat-plate case was exposed to a higher accumulated $\beta(x)$, therefore the large-scale motions in the outer flow were effectively more energized than those in the wing. Nevertheless, it would be expected that the inner peak would also be larger in the $m13$ case, due to the connection between the large-scale motions in the outer flow and the near-wall region, as mentioned above. A possible explanation for this apparent contradiction lies in the use of LES for the $m13$ case, which as also mentioned above does not have a noticeable effect on the outer region. Moreover, in the outer region, the wall-normal and spanwise variances, as well as the Reynolds shear-stress profile, are also stronger in the $m13$ case than in the wing. An alternative explanation might be related to the different upstream histories of the boundary layers exposed to nearly the same β parameter: the boundary layer on the wing increases in terms of the strength of the APG along its downstream evolution, while the TBL in the $m = -0.13$ case stems from a stronger APG that relaxes in terms of β . Whereas the inner layer adapts quickly to the imposed pressure gradient, the outer layer inherits the different upstream histories farther downstream, thereby yielding matched inner-layer turbulence statistics at the same β -value, while the outer layer exhibits amplitudes that are rather representative of the respective β at a more upstream station, *i.e.*, a higher and lower β value for the $m = -0.13$ and wing, respectively.

The second comparison is also between a flat-plate APG and the boundary layer developing on the suction side of the wing, this time at $\beta = 2.9$ and $Re_\tau = 367$. In Figure 6(c) the effect of a stronger APG on the mean flow can be observed in comparison with the ZPG, more precisely, the wake region is significantly stronger (a fact associated with

a much lower skin friction and the lifting up of the boundary layer by the action of the APG), and the incipient log region is steeper. Also in this case, the $\beta(x)$ history from the flat-plate case (*m18*) leads to a higher accumulated effect of the APG in comparison with the wing. In particular, the *m18* case exhibits values of β starting around 2 (at the beginning of the APG region), and increasing up to the value of around 2.9 where the comparison with the wing is performed. On the other hand, in the wing the initial values are around zero and rise quickly up to the value of 2.9, but the accumulated APG effect is significantly inferior to that of the flat-plate case. This is again manifested in the more prominent wake region for the *m18* configuration, due to the fact that the most energetic structures in the outer flow have been exposed to a stronger APG throughout the boundary layer development. The discrepancy in the logarithmic and buffer regions for the streamwise mean velocity profile is larger in this case than what was observed in Figure 6(a), at a lower β . Note that the lower velocities in the buffer region with stronger localized APGs have already been reported by Monty *et al.* (2011), and therefore it is plausible that in this case they could be caused by the different $\beta(x)$ from the two cases. Figure 6(d) further supports the fact that the accumulated $\beta(x)$ in the *m18* case leads to a much more energetic outer region compared with the wing. The outer peak in the streamwise fluctuations is significantly larger in the flat-plate case, and the differences in the outer region are also noticeable in the other two fluctuation components, as well as in the Reynolds shear stress (as opposed to what was observed in the lower β case described above). Interestingly, also in this case the inner peak in the streamwise fluctuations from the two APG TBLs exhibits approximately the same value, despite the large difference in the outer region.

Finally, in Figure 6(e) we compare the mean flow from two flat-plate cases, one with a constant β region (*b2*), and the other one with no constant β (*m16*); both in near-equilibrium. In particular, the comparison is done at $\beta \simeq 2$ and at a higher friction Reynolds number of $Re_\tau = 762$. The effect of the APG is also noticeable in this case, with the more prominent wake and lower velocities in the buffer region, in comparison with the ZPG. Note that the U_∞^+ value from the flat-plate boundary layers is around 30, approximately the value obtained in the *m18* case. This inner-scaled freestream velocity is obtained here with a lower β (2 instead of 2.9), but higher Re_τ (762 instead of 367). This, together with the similarities between Figure 6(f) and d) in terms of inner and outer peaks of the streamwise velocity fluctuations, suggests certain connections between Reynolds-number and pressure-gradient effects. More precisely, a low- Re APG TBL may exhibit features of a high- Re ZPG TBL, if the magnitude of the APG is strong enough. This also points towards certain connections between the energizing mechanisms in the outer flow present at higher Reynolds numbers and with stronger APGs. Focusing on Figure 6(e), it is interesting to note that the two flat-plate cases exhibit very good agreement in their mean flow profiles, although their streamwise developments are different. Nevertheless, Figure 2(b) shows that although the *m16* case exhibits a decreasing trend in $\beta(x)$, and in the *b2* case a region of constant β is observed, from $x \simeq 1500$ to around 2000 (the location where the comparison is done), the two curves converge, and the relative differences between the two curves are below 15%. Hence, both APGs share a similar upstream history for about 6.5 integrated boundary-layer thicknesses. Regarding the components of the Reynolds-stress tensor shown in Figure 6(f), the pressure gradient effects (combined with the moderate Re_τ of 762) lead to significantly more energized structures in the outer region compared with the ZPG, as well as a larger near-wall peak in the streamwise component. Interestingly, in this case the outer peak of the streamwise velocity fluctuations is slightly larger than the inner peak; a phenomenon that suggests the development of a different energy distribution throughout the boundary layer, com-

pared with that of moderately high ZPG TBLs. Such an overtaking of the inner peak by an outer peak has for instance been predicted by the diagnostic profile as shown by Alfredsson *et al.* (2011, 2012), although there, the outer peak resided within the overlap region, which is not the case for strong APGs, cf. Skåre & Krogstad (1994). The other significant observation is the fact that the two flat-plate APG boundary layers exhibit very good agreement in all the components of the Reynolds-stress tensor, again highlighting the convergence of the two boundary layers towards the same state. These results suggest that, in this particular configuration with a moderately changing β , a stream-wise distance of around $x/\delta_0^* \simeq 500$ (where δ_0^* is the displacement thickness of the inflow laminar boundary layer), corresponding to $6.5\bar{\delta}_{99}$, may be sufficient for the APG TBL to become independent of its initial downstream development, and converge towards a certain state uniquely characterized by the β and Re_τ values.

The comparisons presented above were carried out at the same value of the friction Reynolds number as in the work by Harun *et al.* (2013), *i.e.*, they focused on the effect of the pressure-gradient history on TBLs with the same inner-scaled boundary-layer thickness δ_{99}^+ , which fixes the range of scales in the boundary layer. On the other hand, it is important to note that under very strong APG conditions the scales considered in ZPG TBLs are not valid anymore, and therefore the friction Reynolds number would not be an adequate representation of the Reynolds-number effects in the boundary layer. Although this is not the case in the configurations discussed in the present study, it is also interesting to consider cases where the matched Reynolds number is based on a length scale that would also be relevant at stronger APG conditions, such as the displacement thickness. Thus, in Figure 7 we show a comparison between the wing and the *m18* case similar to the one presented in Figure 6(c) and (d), but in this case with a matched value of $\beta = 2.75$ and $Re_{\delta^*} = 2640$. Note that the comparison of inner-scaled mean flow and Reynolds-stress tensor components between the two APG cases is very similar to the one shown in Figure 6, although there is a subtle variation: the difference in APG effect between the *m18* and the wing cases is slightly less pronounced in this matched- Re_{δ^*} comparison. This is due to the fact that when matching Re_τ , the profiles from the two APG cases were extracted at almost the same streamwise position: $x = 841$ in the wing and $x = 852$ in the *m18* boundary layer (cf. Figure 6c)). Nevertheless, when matching Re_{δ^*} the wing profile is extracted slightly downstream ($x = 822$) of the *m18* case ($x = 718$). This is due to the fact that Re_{δ^*} increases more quickly with the APG than Re_τ , since the former is directly connected with the boundary-layer thickness, whereas the latter also includes the reduction in wall-shear stress induced by the APG. Thus, since the *m18* case is subjected to a stronger accumulated effect of $\beta(x)$, it reaches the target Re_{δ^*} earlier than the wing, a fact that also leads to less pronounced APG features with respect to the matched- Re_τ case. Moreover, the most notable difference with respect to Figure 6 is in the ZPG case at matched Re_{δ^*} : although the wake is less prominent, and the outer region of the Reynolds stresses is less energetic than in the APG cases, the δ_{99}^+ values are significantly larger in the ZPG. This can be explained by the fact that the ZPG case only relies on Re -effects to increase the displacement thickness, whereas in the pressure-gradient cases the APG significantly increases it. Thus, the results from the ZPG shown in Figure 6 were obtained at $x = 746$, whereas the ones shown in Figure 7 are obtained at $x = 1757$. The differences in Re_τ values are important in the cases shown in Figure 7: 365 and 332 for wing and *m18*, whereas in the ZPG case the value is 636. This highlights the importance of the different scales when assessing Reynolds-number and pressure-gradient effects, especially in progressively more extreme conditions.

In order to further understand the TKE distribution throughout the boundary layer,

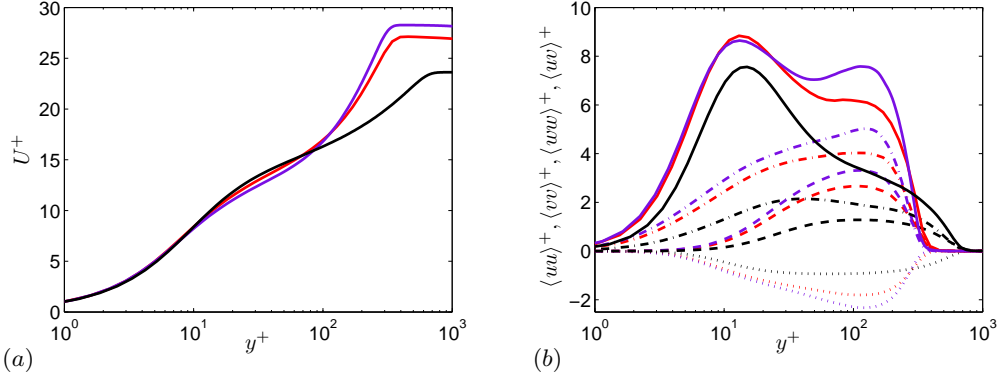


FIGURE 7. (a) Inner-scaled mean velocity profiles and (b) selected components of the inner-scaled Reynolds-stress tensor. Comparison performed at $\beta = 2.75$ and $Re_{\delta^*} = 2640$. Colors and symbols as in Figure 6(c) and (d).

the various terms of the inner-scaled TKE budget, defined in equation (2.2), are shown in Figure 8 for the different cases under consideration, and the same comparisons as in Figure 2 are performed. Note that in the TKE budgets shown in Figure 8 we show the total dissipation, *i.e.*, including the resolved component and also the contribution of the SGS model, as discussed in §2.1. In Figure 8(a) it can be observed that the APG leads to a larger near-wall production peak, as well as to enhanced production throughout the whole boundary layer. Moreover, higher dissipation is observed at the wall in the APG cases. Regarding the differences between the wing and the *m13* case, the accumulated higher $\beta(x)$ from the flat-plate boundary layer leads to higher production in the outer region, as well as to larger dissipation at the wall and in the outer part. With respect to the remaining terms, shown in Figure 8(b), note the higher viscous diffusion at the wall, which compensates the extra wall dissipation in APG TBLs, as well as the point where the turbulent transport changes sign, which also shifts slightly towards the wall. Consequently, the two APG cases exhibit higher values of the velocity-pressure-gradient correlation in the buffer and near-wall regions in comparison with the ZPG, which highlights the relevance of the pressure gradient in the TKE distribution across the boundary layer in the APG case. Interestingly, the most significant difference in this figure between the two APG cases is the higher viscous diffusion in the *m13* configuration, which essentially balances the higher wall dissipation.

The differences between the two APG cases indicated above are magnified when comparing the wing and the *m18* case in Figure 8(c), where not only the high value of $\beta = 2.9$ produces significant discrepancies with respect to the ZPG, but also the very different streamwise development of the two APG boundary layers leads to different manifestations of the pressure gradient effects. The *m18* case exhibits significantly higher production than the wing in the outer region, as well as increased dissipation also in the outer part of the boundary layer. Moreover, the flat-plate case shows higher wall dissipation, and interestingly also a larger value of the inner production peak. This is once again due to the fact that this case has been exposed to a stronger APG over a long streamwise distance, as opposed to the wing. The increased wall dissipation from the *m18* case leads to higher viscous diffusion as observed in Figure 8(d), and also the velocity-pressure-gradient correlation and the turbulent transport are increased in the region $y^+ < 5$. These terms reflect the effect of the APG, especially in the *m18* case which exhibits higher viscous diffusion at

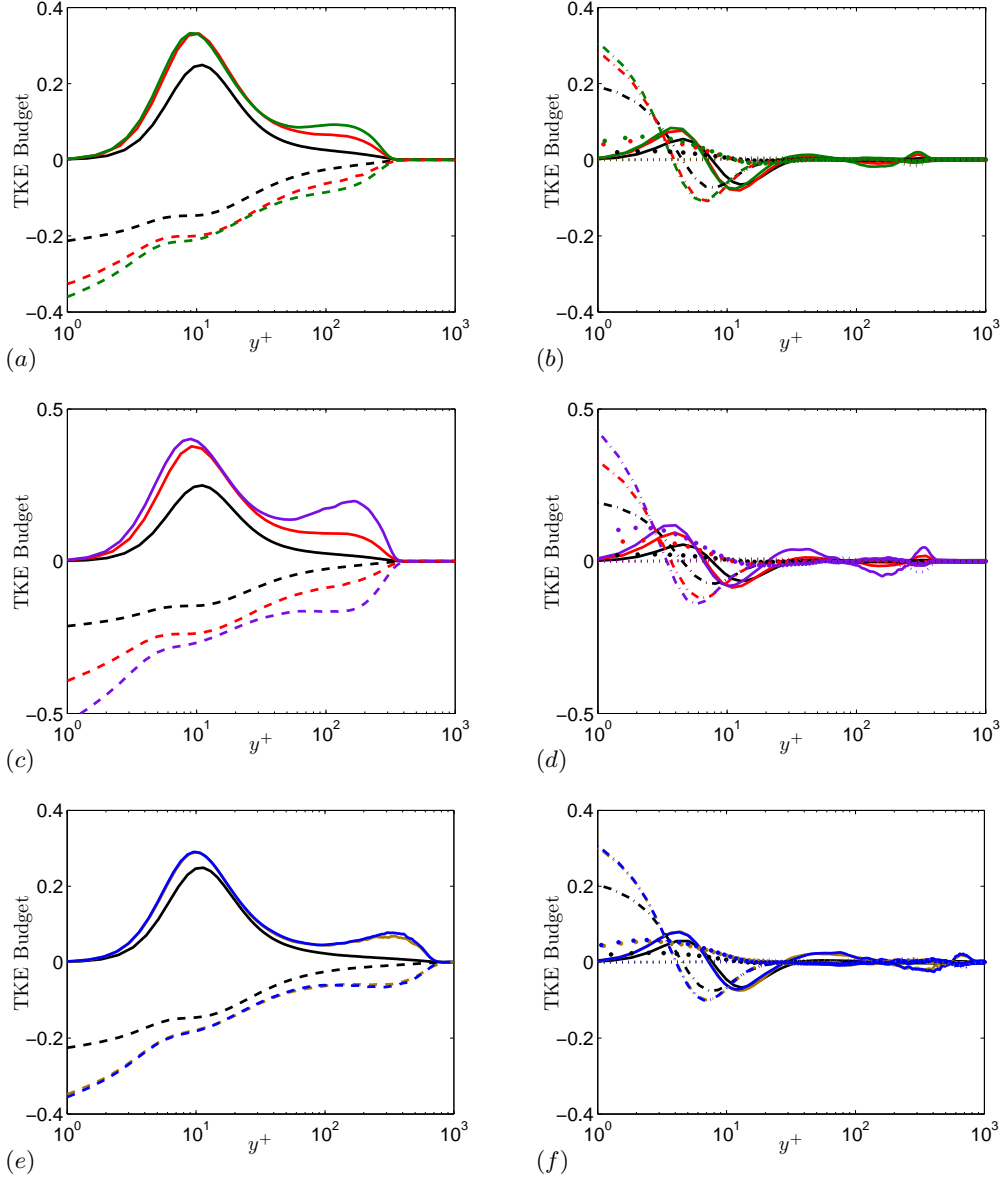


FIGURE 8. (a), (c), (e) Terms of the TKE budget: — production P^k and ---- total dissipation (*i.e.*, the resolved component ε^k plus the contribution from the SGS model in the LES cases); (b), (d), (f) — turbulent transport T^k , --- viscous diffusion D^k , (•) velocity-pressure-gradient correlation Π^t and convection C^k . Cases and colors as in Figure 6. The TKE budget terms are scaled by u_τ^4/ν .

the wall, and larger turbulent transport and velocity-pressure-gradient correlation values close to the wall, than the wing case.

Finally, in Figures 8(e–f) we show the TKE budget terms corresponding to the *m16* and *b2* cases. The previously discussed differences between the APG and ZPG cases, with a β value of 2 and $Re_\tau = 762$, are also present in this case. Thus, we observe higher production and dissipation of TKE throughout the whole boundary layer, especially higher

production in the near-wall peak and outer region, and larger wall dissipation; we also observe higher viscous diffusion at the wall, as well as larger values of the turbulent transport and velocity-pressure-gradient correlation for $y^+ < 5$. Nevertheless, the most remarkable result of these figures is the fact that both flat-plate cases exhibit very good agreement in all the TKE budget terms, again despite of their relatively different upstream histories. As discussed in Figure 6, it appears that a streamwise distance of around $\simeq 6.5\delta_{99}^+$ (over which the differences in β are below 15%) is sufficient for the $m16$ case to converge towards the “canonical” $\beta = 2$ APG TBL, represented in the present study by the $b2$ configuration. Note that in the present context, the statement “canonical” refers to an APG TBL subjected to a constant value of β over its streamwise development. Given the significant impact of the $\beta(x)$ history on the characteristics of an APG TBL, as discussed above, the case with a constant value of β can be considered as a canonical representation of an APG at a given value of β ; this would be analogous to the constant $\beta = 0$ case being the canonical representation of the ZPG TBL. Such convergence to a canonical APG state is a remarkable result, since the TKE budget terms are known for requiring long streamwise convergence lengths (as well as long sampling times). The present results show that it is possible to define a canonical APG turbulent boundary layer case, which is essential for future studies on fundamentals of turbulence in PG TBLs.

As discussed in Figures 6 and 8, the APG energizes the large-scale motions in the outer flow, which leads to larger fluctuations not only in the outer part of the boundary layer, but also in the inner region due to the connection between the structures in the near-wall region and in the outer part of the boundary layer. These statements can be further confirmed by the one-dimensional pre-multiplied spectra of the streamwise velocity shown in Figure 9 for the two non-constant pressure gradient cases with $m = -0.13$ and $m = -0.16$ at matched friction Reynolds number $Re_\tau \simeq 739$. The pre-multiplied streamwise spectra from the ZPG TBL by Schlatter *et al.* (2009) at a similar Re_τ is also shown for comparison. Note that although the domain is not wide enough to completely capture some of the widest structures in the flow, the most relevant structures are properly simulated. The spectral inner peak is found at $y^+ \simeq 12$, $\lambda_z^+ \simeq 120$, a position and width which appears to be approximately independent of the pressure gradient, and in agreement with the higher- Re findings by Eitel-Amor *et al.* (2014). On the other hand, Figure 9 reveals the development of an outer spectral peak with increasing β , which is at the same wall-normal position as the corresponding outer peak observed in all the normal components of the Reynolds stress tensor in Figure 6(f). As mentioned before, the development of this outer peak is caused by the energizing effect of the APG on the most energetic large structures in the flow; a process which shares some similarities with the high- Re behavior in ZPG TBLs. It is in fact interesting to note that this considerable spectral density peak in the outer region is also reported in ZPG TBLs at higher Reynolds number up to $Re_\theta = 8300$ (Eitel-Amor *et al.* 2014), at the same wavelength as the one observed here, *i.e.*, $\lambda_z^+ \simeq 0.8\delta_{99}^+$. This supports the similarities in the development of large-scale motions in the outer region observed at high- Re , and at lower Re but in the presence of an APG.

3.3. Characterization of constant- β APG TBLs

In the previous section we discussed the great impact of flow history in the state of a TBL, and in particular we highlighted the importance of constant- β cases as *canonical* representations of an APG TBL subjected to a certain pressure-gradient magnitude. In this section we characterize the constant- β cases at a matched value of $Re_\tau \simeq 700$. In Figure 10 we show the inner-scaled mean velocity profile and selected components

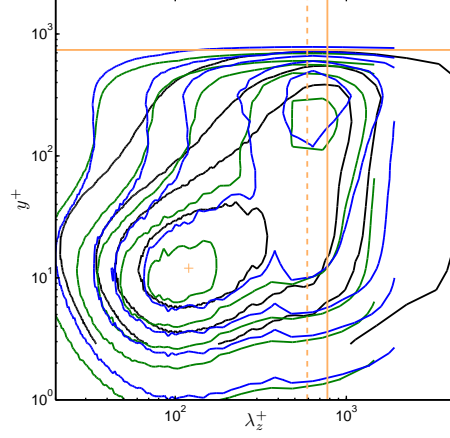


FIGURE 9. Inner-scaled spanwise premultiplied power-spectral density of the streamwise velocity $k_z \Phi_{uu} / u_\tau^2$. The following APG TBL cases are shown: — $m = -0.13$ at $Re_\tau = 763$ and — $m = -0.16$ at $Re_\tau = 739$, and — represents the ZPG TBL case by Schlatter *et al.* (2009) at $Re_\tau = 717$ (black). — denotes $\delta_{99}^+ = 739$, and - - - indicates $\lambda_z^+ = 0.8\delta_{99}^+$. Note that the point $y^+ = 12$, $\lambda_z^+ = 120$ is represented by (+). Isocontour values of 0.1, 0.5, 1 and 2 are shown in the ZPG case, whereas one additional contour with value 3.5 is shown for the $m = -0.13$ and $m = -0.16$ configurations.

of the Reynolds-stress tensor for the cases with constant values of $\beta = 0, 1$ and 2 , *i.e.*, the ZPG and two APG cases. The interest of these configurations lies in the fact that they do not depend on flow history, and therefore can be considered as reference results for the corresponding β cases. Thus, the reported differences among cases are uniquely due to the pressure gradient, and not to flow history. The mean flow profile reveals the more prominent wake (connected to a lower skin-friction coefficient) at larger APGs, and also clearly shows the fact that the buffer layer lies below the one of the ZPG TBL, an effect that becomes more pronounced at progressively larger values of β . As opposed to what is observed in stronger APG conditions (Skåre & Krogstad 1994), the cases under consideration in Figure 10 do not exhibit any differences in the viscous sublayer with respect to the ZPG. As discussed above, the APG also has an important effect in the Reynolds-stress tensor components, manifested in more energetic velocity fluctuation profiles, as well as Reynolds shear-stress profiles. This effect also becomes more pronounced for increasing values of β , and in the $\beta = 2$ case the magnitude of the outer peak in the streamwise velocity fluctuation profile is almost as large as that of the inner peak. An outer peak, which was not present in the ZPG case, also emerges in the other components of the Reynolds-stress tensor, the magnitude of which is proportional to the value of β . Another interesting observation from the Reynolds-stress profiles is the fact that, in the near-wall region, the streamwise and spanwise fluctuation profiles exhibit larger values for progressively stronger APG conditions. This is noticeable already at $y^+ \simeq 2$, and is related to the influence of the more energetic large-scale motions in the outer part of the boundary layer on the near-wall region. Interestingly, these deviations are not present in ZPG TBLs at large Reynolds numbers, a fact that indicates some differences between the energizing mechanisms in TBLs at increasing Re and at increasing β values. Moreover, such differences with pressure gradient are only observed beyond $y^+ \simeq 10$ in the $\langle vv \rangle^+$ and $\langle uv \rangle^+$, a fact that is related to the effect of the wall, which inhibits the wall-normal fluctuations. A summary of the boundary-layer parameters from

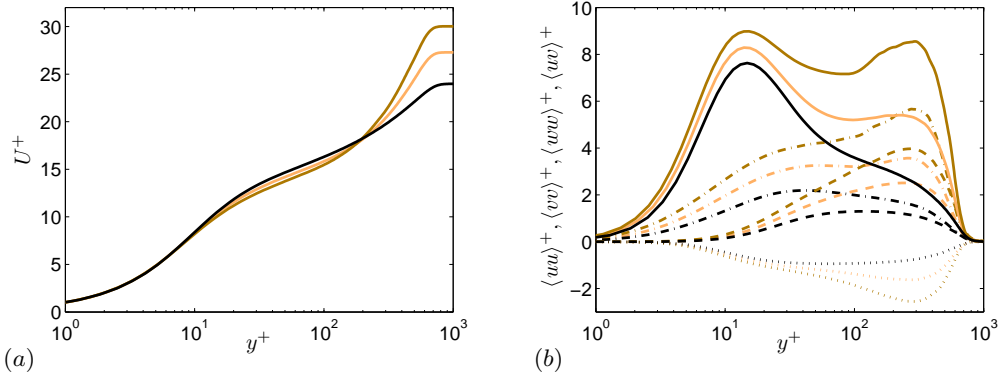


FIGURE 10. (a) Inner-scaled mean velocity profiles and (b) selected components of the inner-scaled Reynolds-stress tensor. Cases with constant values of $\beta = 0, 1$ and 2 , at matched friction Reynolds number $Re_\tau \simeq 700$. Colors as in Table 1 and symbols as in Figure 6.

Value of β	Re_θ	c_f	H_{12}
0	2080	3.5×10^{-3}	1.42
1	2870	2.7×10^{-3}	1.56
2	3360	2.2×10^{-3}	1.68

TABLE 4. Boundary-layer parameters for the cases at matched $Re_\tau \simeq 700$ reported in Figure 10.

the constant- β cases is provided in Table 4, which shows how for the same inner-scaled boundary-layer thickness the Re_θ increases with APG, a manifestation of the thickening of the TBL due to its deceleration. The APG also leads to lower skin-friction coefficients (as the boundary layer thickens, the velocity gradient at the wall is reduced), as well as to larger values of the shape factor (connected to the larger displacement thickness resulting from the APG).

4. Assessment of alternative scaling laws

Due to the significant impact of history effects on the local flow features discussed throughout §3, here we aim at characterizing the scaling in the configurations with values of β constant over a significant portion of the domain, discussed in §3.3. As observed by Mellor & Gibson (1966), the constant β configuration is a particular case of a near-equilibrium TBL, and therefore the $U_\infty(x)$ distribution is also defined by a power law with particular choices of x_0 and m . A detailed characterization of constant β cases will ultimately allow to assess pressure-gradient effects with progressively more complex history effects, given by the particular $\beta(x)$ distribution. In Figure 11 we show a schematic representation of the $b1$ case, and of the region in the computational domain where the constant value of $\beta = 1$ is observed. In this figure it is shown that the $\beta = 1$ region spans from $x/\delta_0^* = 500$ to 2300 , which corresponds to a Reynolds-number range of $950 < Re_\theta < 3255$. As discussed in §2, this corresponds to around 37 averaged boundary-

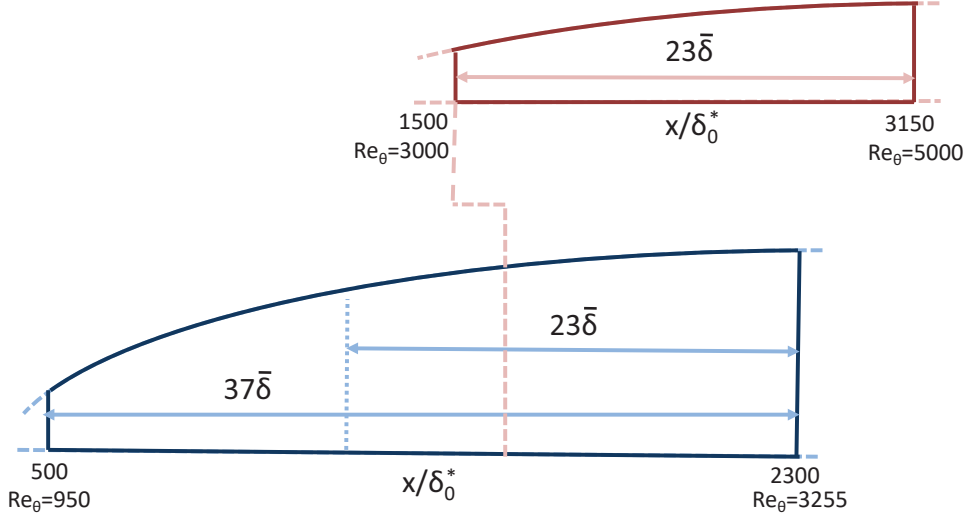


FIGURE 11. — Sketch of the b1 APG TBL case showing the area where a constant value of $\beta = 1$ was obtained, where δ_0^* is the displacement thickness of the laminar inflow boundary layer. — Domain of interest with $\beta = 1$ extracted from the study by Kitsios *et al.* (2016). The extent of the constant $\beta = 1$ regions are shown in both cases normalized with the averaged boundary-layer thicknesses $\bar{\delta}$. The extent of the domain of interest from Kitsios *et al.* (2016) is also represented in our case. The dashed line connecting both domains indicates the streamwise distance where the region of constant β starts in the simulation by Kitsios *et al.* (2016), *i.e.*, $x/\delta_0^* = 1500$.

layer thicknesses, where the streamwise average is taken over the constant- β range. This figure also shows the region of constant $\beta = 1$ observed in the simulation by Kitsios *et al.* (2016), which in their case spans from $x/\delta_0^* = 1500$ to 3150, a range that corresponds to $3000 < Re_\theta < 5000$. Note that although in the simulation by Kitsios *et al.* (2016) the Reynolds-number range is higher than the one considered in the present study, their region of constant β spans a streamwise distance of only 23 averaged boundary-layer thicknesses, *i.e.*, a distance 1.6 times shorter than the one considered in the present simulation.

Figures 12(a) and (b) show the inner-scaled mean flow and velocity fluctuations corresponding to case b1, schematically discussed in Figure 11. The profiles within the region of constant $\beta = 1$ are highlighted in the two panels. The mean flow shows all characteristic features of APG TBLs, as discussed in §3. Moreover, the velocity fluctuations develop an outer peak in all components, connected with the most energetic structures in the outer region. An alternative scaling for these quantities was considered by Kitsios *et al.* (2016) in their simulation, based on the displacement thickness δ^* and the local edge velocity U_e . They observed an apparent collapse of the mean flow and the fluctuations in their region of constant β , which as indicated in Figure 11 corresponds to a streamwise distance of around 23 integrated boundary-layer thicknesses $\bar{\delta}$. In Figures 12(c) and (d) we apply the same scaling to our data: as apparent no such collapse in any of the investigated quantities in our constant β region, which spans a longer streamwise distance of $37\bar{\delta}$, is observable. One possible explanation for this discrepancy could be that the scaling considered by Kitsios *et al.* (2016) does not lead to self-similarity, and since their constant β region is shorter than ours and their Re -range spans a shorter fraction of a decade, their streamwise development would be insufficient to reveal this conclusion.

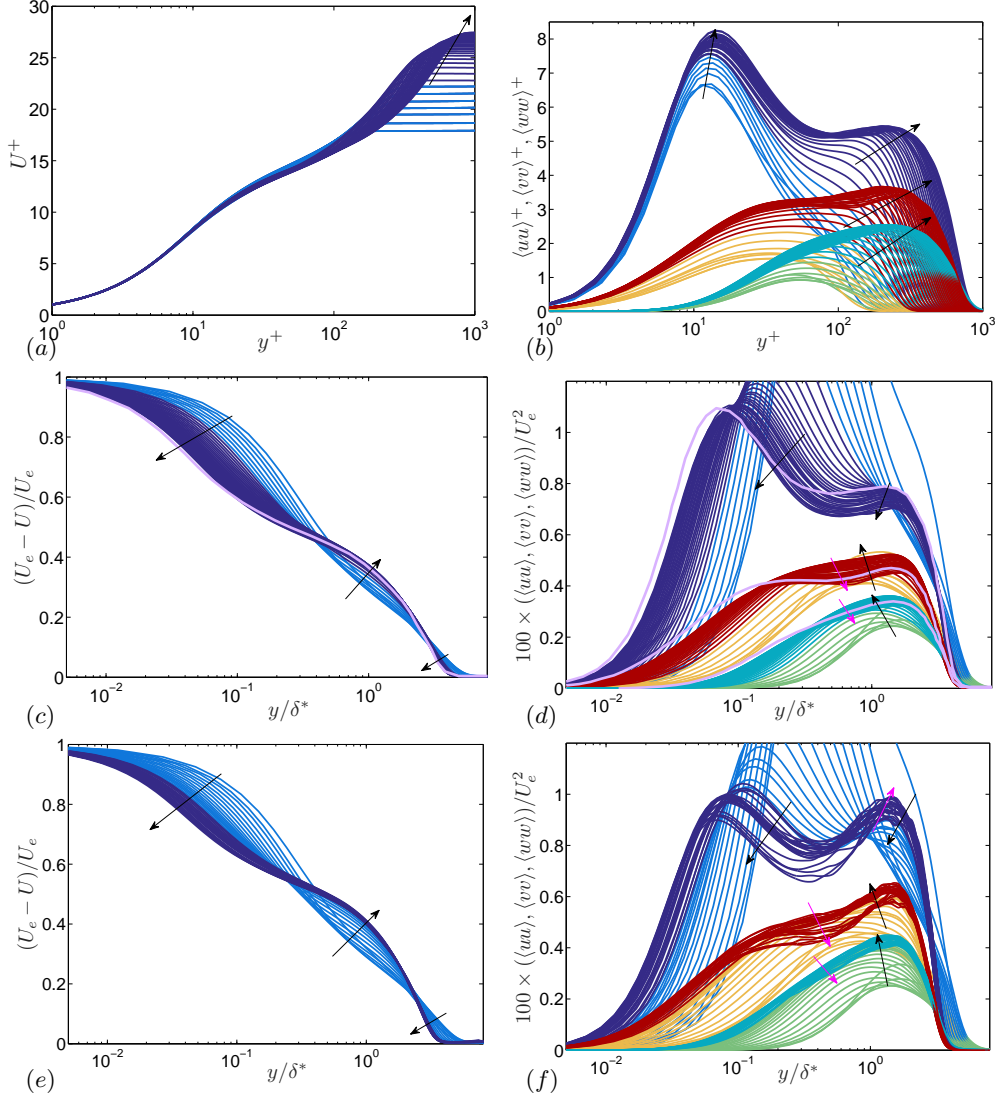


FIGURE 12. Case $\beta = 1$: mean streamwise velocity profiles and selected Reynolds-stress tensor components (31 profiles in the range $100 < x < 2300$) non-dimensionalised by (a), (b) u_τ and $\ell^* = \nu/u_\tau$, and (c), (d) U_e and δ^* . — indicates profiles in the area of constant β for U and $\langle uu \rangle$, whereas — denotes profiles where β is not constant. — and — denote profiles of $\langle vv \rangle$ and $\langle ww \rangle$ within the constant β region, whereas — and — correspond to profiles without constant β . Average of collapsed profiles reported by Kitsios *et al.* (2016) represented by —. Case $\beta = 2$: (e) mean streamwise velocity profiles (23 positions in the range $100 < x < 2300$), and (f) selected Reynolds-stress tensor components, with same scaling and color code as in (c) and (d). The black arrows indicate the evolution of various parts of the profiles with increasing Reynolds number. The magenta arrows are included in the cases where a change in the trend is produced, in which case the magenta arrow indicates the new evolution of the profiles with Re .

The present data exhibits a clear Re trend, which is furthermore extended through the higher Re data by Kitsios *et al.* (2016). The failure of the scaling would indeed be in agreement with Townsend (1956), since in principle the sink flow is the only flow that can be described from the wall to the freestream in terms of a single similarity variable in y . It is also interesting to note that recent particle image velocimetry (PIV) experiments performed in a similar configuration to that of Kitsios *et al.* (2016), carried out by the same research group (Atkinson *et al.* 2016), also shows Re -dependent profiles of the Reynolds-stress tensor components. These aspects are further explored by analyzing the constant $\beta = 2$ case, over a streamwise distance of 28δ . Note that the region of constant $\beta = 2$ found in the $b2$ case is located in $1000 < x/\delta_0^* < 2300$. A higher Re_θ range is reached in this case, which is more comparable to the one analyzed by Kitsios *et al.* (2016), albeit at a higher value of β . As seen from Figures 12(e) and (f), the scaling by Kitsios *et al.* (2016) does not lead to self-similarity in this case either. Also here a clear Re trend is noticed, supporting the statements presented above, and also the validity of the classic two-layer similarity, at least for the β range under consideration.

5. Conclusions

The present study is focused on the history effects in turbulent near-equilibrium boundary layers with pressure gradients. After defining the *near-equilibrium* state according to Townsend (1956), large-eddy simulations were performed over a flat plate to assess the effect of different evolutions of the pressure-gradient parameter β . The adverse pressure gradient was imposed by a varying freestream velocity profile at the top of the domain, *i.e.*, in the freestream. Hereby constant and non-constant pressure-gradient-parameter distributions were achieved. With the constant values of β , turbulent boundary layers at a certain state can be investigated over a certain Re -range. In this case, the skin-friction coefficient and shape factor distributions appear nearly parallel to those of their ZPG counterpart, which is a special case of a near-equilibrium ($\beta = 0$) TBL. An interesting finding was obtained when comparing the mean and Reynolds-stress profiles of the non-constant pressure and constant APG TBLs at matched β and Re_τ . The non-constant β case appears to converge towards the canonical state after a sufficiently long downstream length. For the conditions investigated in the present study, this length is $7\delta_{99}$, a conclusion that was also confirmed by inspection of the TKE budget.

The history effects were studied not only in flat-plate TBLs, but also in the APG boundary layer developing over the suction side of a NACA4412 wing section. The large structures in the outer region were found to be less energetic (in inner scaling) on the suction side of the wing than in the flow over the flat plate for matched β and Re_τ . The structures were exposed to a lower PG throughout the streamwise development of the boundary layer (compared to the ones over the flat plate), resulting in a less pronounced wake region and a less intense outer region in the Reynolds stresses. The TKE budget also shows some of the reported effects of the APG, such as the higher values in the velocity-pressure-gradient correlation in the buffer and near-wall region or the extra wall dissipation. The comparison between the flow over a wing and the flat plate led to interesting results, such as the fact that the viscous diffusion term is stronger close to the plate than over the surface of the wing at same β . This is due to the stronger wall dissipation resulting from the larger accumulated effect of the β history. One-dimensional spectral density maps indicate that the large-scale structures are energized in APG TBLs compared to ZPG TBLs at matched friction Reynolds numbers. The position of the near-wall spectral peak appears to be independent of the APG.

Although some similarities can be drawn between PG TBLs and high- Re ZPG TBLs

in terms of the mechanisms by which the large-scale motions are energized, additional work must be carried out over a wide range of Reynolds-number and pressure-gradient conditions in order to clearly assess the combined effect of both on the characteristics of TBLs.

Finally, we investigated the scaling proposed by Kitsios *et al.* (2016), in which δ^* and U_e are considered as length and velocity scales. Our results show that this scaling does not lead to self-similar boundary layer profiles in the constant β region. This conclusion is in agreement with Townsend (1956), who showed that the sink flow is the only boundary layer exhibiting self-similarity. Although the current flat-plate simulations established long constant β regions, stronger streamwise constant pressure gradients at higher Reynolds numbers should be investigated in order to characterise cases closer to wind-tunnel experiments and general applications.

Acknowledgements

Financial support provided by the Knut and Alice Wallenberg Foundation and the Swedish Research Council (VR) is gratefully acknowledged. The simulations were performed on resources provided by the Swedish National Infrastructure for Computing (SNIC) at the PDC Center for High Performance Computing at KTH Stockholm.

REFERENCES

- ALFREDSSON, P. H., ÖRLÜ, R. & SEGALINI, A. 2012 A new formulation for the streamwise turbulence intensity distribution in wall-bounded turbulent flows. *Eur. J. Mech. B/Fluids* **36**, 167–175.
- ALFREDSSON, P. H., SEGALINI, A. & ÖRLÜ, R. 2011 A new scaling for the streamwise turbulence intensity in wall-bounded turbulent flows and what it tells us about the “outer” peak. *Phys. Fluids* **23**, 041702.
- ATKINSON, C., BUCHNER, A. J., EISELDER, M., KITSIOS, V. & SORIA, J. 2016 Time-resolved PIV measurements of a self-similar adverse pressure gradient turbulent boundary layer. In *Proc. 18th Intl Symp. on the Application of Laser and Imaging Techniques to Fluid Mechanics, Lisbon, Portugal*.
- BAILEY, S. C. C., HULTMARK, M., MONTY, J. P., ALFREDSSON, P. H., CHONG, M. S., DUNCAN, R. D., FRANSSON, J. H. M., HUTCHINS, N., MARUSIC, I., MCKEON, B. J., NAGIB, H. M., ÖRLÜ, R., SEGALINI, A., SMITS, A. J. & VINUESA, R. 2013 Obtaining accurate mean velocity measurements in high Reynolds number turbulent boundary layers using Pitot tubes. *J. Fluid Mech.* **715**, 642–670.
- BOBKE, A., ÖRLÜ, R. & SCHLATTER, P. 2016a Simulations of turbulent asymptotic suction boundary layers. *J. Turbul.* **17**, 155–178.
- BOBKE, A., VINUESA, R., ÖRLÜ, R. & SCHLATTER, P. 2016b Large-eddy simulations of adverse pressure gradient turbulent boundary layers. *J. Phys.: Conf. Ser.* **708**, 012012.
- CHEVALIER, M., SCHLATTER, P., LUNDBLADH, A. & HENNINGSON, D. S. 2007 A pseudospectral solver for incompressible boundary layer. Technical Report TRITA-MEK 2007:07. KTH Mechanics.
- EITEL-AMOR, G., ÖRLÜ, R. & SCHLATTER, P. 2014 Simulation and validation of a spatially evolving turbulent boundary layer up to $Re_\theta = 8300$. *Int. J. Heat Fluid Flow* **47**, 57–69.
- FISCHER, P. F., LOTTES, J. W. & KERKEMEIER, S. G. 2008 NEK5000: Open source spectral element CFD solver. Available at: <http://nek5000.mcs.anl.gov>.
- HARUN, Z., MONTY, J. P., MATHIS, R. & MARUSIC, I. 2013 Pressure gradient effects on the large-scale structure of turbulent boundary layers. *J. Fluid Mech.* **715**, 477–498.
- HOSSEINI, S. M., VINUESA, R., SCHLATTER, P., HANIFI, A. & HENNINGSON, D. S. 2016 Direct numerical simulation of the flow around a wing section at moderate Reynolds number. *Int. J. Heat Fluid Flow* **61**, 117–128.

- HUTCHINS, N., NICKELS, T. B., MARUSIC, I. & CHONG, M. S. 2009 Hot-wire spatial resolution issues in wall-bounded turbulence. *J. Fluid Mech.* **635**, 103–136.
- KITSIOS, V., ATKINSON, C., SILLERO, J. A., BORRELL, G., GUNGOR, A. G., JIMÉNEZ, J. & SORIA, J. 2016 Direct numerical simulation of a self-similar adverse pressure gradient turbulent boundary layer. *Int. J. Heat Fluid Flow* **61**, 129–136.
- LEE, J. H. 2017 Large-scale motions in turbulent boundary layers subjected to adverse pressure gradients. *J. Fluid Mech.* **810**, 323–361.
- LEE, J. H. & SUNG, H. J. 2009 Structures in turbulent boundary layers subjected to adverse pressure gradients. *J. Fluid Mech.* **639**, 101–131.
- MACIEL, Y., ROSSIGNOL, K.-S. & LEMAY, J. 2006 Self-Similarity in the outer region of adverse-pressure-gradient turbulent boundary layers. *AIAA J.* **44**, 2450–2464.
- MARUSIC, I., CHAUHAN, K. A., KULANDAIVELU, V. & HUTCHINS, N. 2015 Evolution of zero-pressure-gradient boundary layers from different tripping conditions. *J. Fluid Mech.* **783**, 379–411.
- MARUSIC, I., MCKEON, B. J., MONKEWITZ, P. A., NAGIB, H. M., SMITS, A. J. & SREENIVASAN, K. R. 2010 Wall-bounded turbulent flows at high Reynolds numbers: Recent advances and key issues. *Phys. Fluids* **22**, 065103.
- MELLOR, G. L. & GIBSON, D. M. 1966 Equilibrium turbulent boundary layers. *J. Fluid Mech.* **24**, 225–253.
- MONKEWITZ, P. A., CHAUHAN, K. A. & NAGIB, H. M. 2007 Self-consistent high-reynolds-number asymptotics for zero-pressure-gradient turbulent boundary layers. *Phys. Fluids* **19**, 115101.
- MONTY, J. P., HARUN, Z. & MARUSIC, I. 2011 A parametric study of adverse pressure gradient turbulent boundary layers. *Int. J. Heat Fluid Flow* **32**, 575–585.
- NAGIB, H. M. & CHAUHAN, K. A. 2008 Variations of von Kármán coefficient in canonical flows. *Phys. Fluids* **20**, 101518.
- NAGIB, H. M., CHAUHAN, K. A. & MONKEWITZ, P. A. 2007 Approach to an asymptotic state for zero pressure gradient turbulent boundary layers. *Phil. Trans. R. Soc. A* **365**, 755–770.
- PERRY, A. E., MARUSIC, I. & JONES, M. B. 2002 On the streamwise evolution of turbulent boundary layers in arbitrary pressure gradients. *J. Fluid Mech.* **461**, 61–91.
- SCHLATTER, P. & ÖRLÜ, R. 2010 Assessment of direct numerical simulation data of turbulent boundary layers. *J. Fluid Mech.* **659**, 116–126.
- SCHLATTER, P. & ÖRLÜ, R. 2012 Turbulent boundary layers at moderate Reynolds numbers. Inflow length and tripping effects. *J. Fluid Mech.* **710**, 5–34.
- SCHLATTER, P., ÖRLÜ, R., LI, Q., BRETHOUWER, G., FRANSSON, J. H. M., JOHANSSON, A. V., ALFREDSSON, P. H. & HENNINGSON, D. S. 2009 Turbulent boundary layers up to $Re_\theta = 2500$ studied through simulation and experiment. *Phys. Fluids* **21**, 051702.
- SCHLATTER, P., STOLZ, S. & KLEISER, L. 2004 LES of transitional flows using the approximate deconvolution model. *Int. J. Heat Fluid Flow* **25**, 549–558.
- SKOTE, M. 2001 Studies of turbulent boundary layer flow through direct numerical simulation. *Ph. D. thesis, Royal Institute of Technology, Stockholm, Sweden*.
- SKOTE, M. & HENNINGSON, D. S. 2002 Direct numerical simulation of a separated turbulent boundary layer. *J. Fluid Mech.* **471**, 107–136.
- SKOTE, M., HENNINGSON, D. S. & HENKES, R. A. W. M. 1998 Direct numerical simulation of self-similar turbulent boundary layers in adverse pressure gradients. *Flow Turbul. Combust.* **60**, 47–85.
- SKÅRE, P. E. & KROGSTAD, P.-Å. 1994 A turbulent equilibrium boundary layer near separation. *J. Fluid Mech.* **272**, 319–348.
- SPALART, P. R. & WATMUFF, J. H. 1993 Experimental and numerical study of a turbulent boundary layer with pressure gradients. *J. Fluid Mech.* **249**, 337–371.
- TOWNSEND, A. A. 1956 The Structure of Turbulent Shear Flow. *Cambridge Univ. Press, Cambridge, UK*.
- VINUESA, R., BOBKE, A., ÖRLÜ, R. & SCHLATTER, P. 2016 On determining characteristic length scales in pressure-gradient turbulent boundary layers. *Phys. Fluids* **28**, 055101.
- VINUESA, R., ÖRLÜ, R. & SCHLATTER, P. 2017 Characterisation of backflow events over a wing section. *J. Turbul.* **18**, 170–185.

- VINUESA, R., ROZIER, P. H., SCHLATTER, P. & NAGIB, H. M. 2014 Experiments and computations of localized pressure gradients with different history effects. *AIAA J.* **55**, 368–384.